Biophysical Journal
Article

Biophysical Society

Multimodal microscale mechanical mapping of cancer cells in complex microenvironments

Miloš Nikolić,[1,2] Giuliano Scarcelli,[2,3] and Kandice Tanner[1,*]
[1]Laboratory of Cell Biology, Center for Cancer Research, National Cancer Institute, National Institutes of Health, Bethesda, Maryland; [2]Maryland Biophysics Program, IPST, University of Maryland, College Park, Maryland; and [3]Fischell Department of Bioengineering, University of Maryland, College Park, Maryland

ABSTRACT The mechanical phenotype of the cell is critical for survival following deformations due to confinement and fluid flow. One idea is that cancer cells are plastic and adopt different mechanical phenotypes under different geometries that aid in their survival. Thus, an attractive goal is to disrupt cancer cells' ability to adopt multiple mechanical states. To begin to address this question, we aimed to quantify the diversity of these mechanical states using in vitro biomimetics to mimic in vivo two-dimensional (2D) and 3D extracellular matrix environments. Here, we used two modalities Brillouin microscopy (~GHz) and broadband frequency (7–15 kHz) optical tweezer microrheology to measure microscale cell mechanics. We measured the response of intracellular mechanics of cancer cells cultured in 2D and 3D environments where we modified substrate stiffness, dimensionality (2D versus 3D), and presence of fibrillar topography. We determined that there was good agreement between two modalities despite the difference in timescale of the two measurements. These findings on cell mechanical phenotype in different environments confirm a correlation between modalities that employ different mechanisms at different temporal scales (Hz-kHz versus GHz). We also determined that observed heterogeneity in cell shape is more closely linked to the cells' mechanical state. Moreover, individual cells in multicellular spheroids exhibit a lower degree of mechanical heterogeneity when compared with single cells cultured in monodisperse 3D cultures. The observed decreased heterogeneity among cells in spheroids suggested that there is mechanical cooperativity between cells that make up a single spheroid.

SIGNIFICANCE Mechanical phenotype is defined by treating the cell as a material. It is a key parameter, as it determines the interplay between forces (e.g., tension, compressive pressure, confinement) and the resultant changes in cell morphology such as shape and size. This phenotype may be linked to determinants of the onset and progression of cancer. Malignant cells might adopt various mechanical states as they encounter different environments. To identify which properties of the external cell microenvironment direct changes in cell mechanical phenotype, we measured the mechanical properties of single cells using two optical methods (Brillouin microscopy and high-frequency optical tweezer microrheology). We combined these methods with in vitro biomimetic 2D and 3D microenvironment fabrication to probe cell mechanics in microenvironmental contexts that are difficult to investigate with traditional contact-based microrheology methods.

INTRODUCTION

Cancer cells encounter many different biochemical and physical cues within the organ microenvironment. These cues are anisotropic and undergo temporal evolution within the microenvironment milieu (1). As part of an intricate feedback mechanism, cancer cells sense environmental cues, which evokes a modulation in cellular behavior, which in turn regulates secretion of extracellular cytokines, alterations in tissue architecture, and remodeling of cell mechanics (1,2). Thus, there is an emergence of distinct microenvironments during cancer progression. Simply, the cues at a stage of transition from normal to malignant may be distinct from those present at stages of invasive growth into surrounding tissues due to the continuous tissue remodeling. (2,3). Understanding the interplay between dynamic tissue reciprocity and the emergence of heterogeneous cell phenotypes is critical for our understanding of why some cancer cells remain indolent and why some are aggressively invasive.

Submitted April 4, 2022, and accepted for publication September 2, 2022.
*Correspondence: kandice.tanner@nih.gov
Editor: Guy Genin.
https://doi.org/10.1016/j.bpj.2022.09.002

This dynamic reciprocal cross talk may also drive phenotypic changes that might select for clones with enhanced survival, motility, and drug resistance (4–8). These phenotypes can be classified by genetic, metabolic, and physical traits (9,10). The latter is often referred to as the mechanical phenotype. The cellular constituents spanning a multiplicity of length scales, enzymatic activity, and cell-cycle stage collectively regulate the physical phenotype of the cell (11). In the last decade, mechanical phenotypes have been posited as critical determinants of cancer progression (12–18). Specifically, the mechanical phenotype can regulate a cell's response to external forces such as those encountered during invasion and transit within conduits during circulation (19,20). Mechanical phenotype also is an important determinant of motility strategies such as ameboid-, mesenchymal-, and "piston"--driven modes of migration that are needed to navigate complex three-dimensional (3D) structures (21,22). Finally, mechanical phenotype also influences the homotypic and heterotypic cell-cell interactions that occur within the tumor and interactions with stromal and immune cells (23,24). These cellular couplings, such as cancer cell-cancer-associated fibroblasts, cancer cell-cancer-associated macrophages, and clusters of cancer cells, have all been shown to facilitate tumor outgrowth, escape, invasion, extravasation, and colonization of distant organs (25). Our understanding of the environmental regulation of these states necessitates technical expertise to resolve mechanical phenotypes in complex environments.

The mechanical phenotype can be defined by several metrics such as a viscoelasticity, cell shape, cell deformability, and adhesion properties. Of these metrics, single-cell viscoelasticity provides a metric to assess the material properties of individual cells. Microrheology is a common metric that is used to quantify material properties (26–28). These material properties are defined by combinatorial contributions due to cellular components that show energy dissipation and elastic properties. Novel tools such as atomic force microscopy, optical tweezers, magnetic twisting cytometry, and micropipette aspiration have been utilized for characterization of cellular material properties (10,29,30). However, it remains technically difficult to assess cells in complex environments with microscale resolution. To address this technical need, we methodically probed the single-cell mechanics for a range of in vitro assays as a function of dimension, anisotropy, and multicellular organization using two optical-based techniques that can access the mechanical properties of cells in complex 3D environments. We employed Brillouin microscopy (31,32), which is sensitive to material properties at the GHz timescale, and broadband frequency multiplexed optical tweezer microrheology (7–15 kHz) (33,34). These techniques allowed us to probe microscale mechanical properties and serve as a platform for comparative studies at the same length scale in different frequency regimes.

MATERIALS AND METHODS

Cell culture

Human glioblastoma cells U87 (ATCC HTB-14) were obtained from ATCC, MCF10CA1h cells (35) were received from the Barbara Ann Karmanos Cancer Institute (Detroit, MI, USA), and they were cultured as previously described. Briefly, the U87 cells were cultured in Dulbecco's modified Eagle medium (Thermo Fisher Scientific, Waltham, MA, USA, 11995065) that was supplemented with 10% fetal bovine serum (Thermo Fisher Scientific, 11995065) and 50 U/mL penicillin and 50 μg/mL streptomycin (Thermo Fisher Scientific, 15070-063). MCF10CA1h cells were cultured in the complete medium: Dulbecco's modified Eagle medium/F12 (11330-032, Thermo Fisher Scientific); 5% horse serum (16050-122, Thermo Fisher Scientific); 5 ng/mL EGF (AF-100-15-1MG, Peprotech, East Windsor, NJ, USA); 0.5 mg/mL hydrocortisone (H0888-1G, Sigma-Aldrich, Burlington, MA, USA); 100 ng/mL cholera toxin (C8052-2mg, Sigma-Aldrich); 10 μg/mL insulin (I1882-100MG, Sigma-Aldrich); and 1$\times$ penicillin/streptomycin solution (15070-063, Thermo Fisher Scientific). Cells were cultured at 37°C in 5% CO_2. Cell propagation was performed by detaching adherent cells using Trypsin (0.25% for U87 cells; Thermo Fisher Scientific, 80-2101) and 0.05% for MCF10CA1h cells (25-052-Cl, Corning, Corning, NY, USA) as previously described. All experiments were performed using cells with passage numbers less than 19. Cell medium was changed every 2–3 days.

Preparation of polyacrylamide substrates

Polyacrylamide gels of varying stiffness were fabricated using previously reported protocols (36). Briefly, 35 mm glass-bottom dishes (Ibidi, Fitchburg, WI, USA, 81158) were incubated with 0.1 M sodium hydroxide (Sigma-Aldrich, 72068). Then, 200 μL APTMS was added to the dishes for 3 min (Sigma-Aldrich, 281778), followed by 400 μL 0.5% glutaraldehyde for 30 min (Sigma-Aldrich, G6257) to ensure polyacrylamide attachment to the treated glass. The stiffness of polyacrylamide gels can be altered by tuning the relative ratios of acrylamide to bis-acrylamide. First, a mixture of 40% acrylamide (Sigma-Aldrich, A4058-100 mL), 2% bis-acrylamide (Sigma-Aldrich M1533-25 mL), phosphate-buffered saline (PBS) (Thermo Fisher Scientific, 14190-144), TEMED (Sigma-Aldrich, T7024-25 mL), and 10% w/v ammonium persulfate (Sigma-Aldrich, 215589) were thoroughly mixed. In these experiments, we fabricated gels that corresponded to a shear modulus (G') of 0.1 (soft gels) and 32 kPa (stiff gels). For soft gels, the final concentrations were 5% acrylamide and 0.04% bis-acrylamide. For stiff gels, the final solution contained 18% acrylamide and 0.4% bis-acrylamide. In each case, a total volume of 500 μL was prepared. 30 μL gel solution was added to the pre-treated 35 mm glass-bottom dish and covered with 18 mm round coverslips (#1, thickness) to create a circular gel. This coverslip was pre-treated with RainX (Illinois Tool Works, Glenview, IL, USA) for 5 min to make them less adhesive to the polyacrylamide gels. After 15 min, 2 mL PBS was added to the dish. After an additional 15 min, the glass coverslip was gently dislodged using tweezers, leaving a polyacrylamide gel $\sim$100 μm in thickness.

Cells do not attach to biologically inert polyacrylamide and require coating the gel surface with an extracellular matrix protein to promote attachment. First, the polyacrylamide gels were treated with 0.25 mg/mL Sulfo-SANPAH (Thermo Fisher Scientific) in 50 mM HEPES (Thermo Fisher Scientific). They were coated with 200 μL sulfo-SANPAH solution and placed under the UV lamp (UVP, Blak-Ray B100AP, 100 W, 365 nm) for 6 min. This step was repeated twice. The gels were then gently washed with 50 mM HEPES buffer twice and covered with a solution of fibronectin (Milipore Sigma FN010; 10 μg/mL) in HEPES for 12 h at 4°C. Afterward, the gels were washed twice with PBS. Next, 2 mL solution of 50,000 cells in the serum-free medium was added to the gels. Gels were then placed in the incubator overnight to facilitate cell attachment.

Preparation of cells on 2D and in 3D culture

Cells cultured on top (2D) and embedded in 3D laminin-rich extracellular matrix were prepared as previously described (37). Briefly, we coated the bottom of a chilled 4 well μ-Slide (Ibidi, 80427) with 100 μL ice-cold Matrigel (Corning, 356231, lot 8232015). The slide was then incubated at 37°C for 5 min for the Matrigel layer to solidify. For seeding cells in 2D, 50,000 cells were added directly to the well in 500 μL serum-free medium. For seeding cells in 3D, 430 μL Matrigel was mixed on ice with 50 μL 2×10^6 cells/mL solution of cells (10^5 cells total) in serum-free medium and 12 μL of serum-free cell medium. The mixture was added on top of the previously gelled layer of Matrigel and incubated at 37°C for 30 min for complete gelation. After 30 min, 350 μL serum-free medium was added each well. Cells were used imaged the following day.

Preparation of fibrillar topography (FT) in 3D culture

Aligned magnetic self-assembled fibrillar matrices were fabricated using a previously reported protocol (37–39). First, human fibronectin (Milipore Sigma, FN010) was fluorescently labeled using the DyLight 488 Microscale Labeling Kit (Thermo Fisher Scientific, 53024) according to the supplier protocol. Concentration of the fluorescently labeled protein was measured using a spectrophotometer (Nanodrop 2000c) and kept for up to 4 weeks at 4°C. Fluorescently labeled human fibronectin was conjugated to the carboxylated magnetic polystyrene beads (Ademtech Carboxy-Adembeads Coupling Kit, Ademtech, Pessac, France, 02820) according to the manufacturer protocol. Magnetic beads of 300 nm diameter were washed three times in the activation buffer. The beads were resuspended at the concentration of 0.5 mg/100 μL. Activation of the beads was achieved by incubation in a 2 mg/mL solution of EDC at room temperature for 1 h. Then, 20 μg fluorescently labeled protein was added to 100 μL of the activated beads and incubated at room temperature overnight under gentle shaking. The next day, the conjugated beads were washed three times with storage buffer and kept at 4°C for up to 1 week at a concentration of 10 mg/mL.

The FT in 3D sample was prepared similarly to the 3D Matrigel encapsulation of cells as described above. 430 μL ice-cold Matrigel was mixed with 12 μL FN-conjugated beads (10 mg/mL) and 50 μL of the cell solution (total 10^5 cells in serum-free medium) and added to the well of the 4-well Ibidi slide that had a layer of 100 μL Matrigel previously polymerized on the bottom. To induce alignment, the slide was then placed on ice-cold magnet (KJ Magnetics, Pipersville, PA, USA, BX8×8X8-N52) for 15 min. After 15 min, the beads assembled in a FT. The sample was then immediately placed in the incubator at 37°C for 30 min for Matrigel to solidify. Afterward, 350 μL serum-free medium was added to the well. A control sample (FT control) was prepared in the same way, but incubated on ice for 15 min, in a separate ice bucket. The FN-conjugated magnetic beads were uniformly dispersed through the 3D gel for the FT control sample.

Sample preparation for optical tweezer experiments

Cells were detached from the culture flask using 10 mM EDTA solution. Cells were resuspended in fresh medium at concentration of 1.5×10^6 cells/mL. Cells were then mixed with a solution of polystyrene beads (1 μm diameter, 2% solids, Invitrogen, Waltham, MA, USA, F8816) in a proportion of 100 μL beads/500 μL cell solution and incubated at 37°C, 5% CO_2, for 30 min with gentle mixing for 30–45 min at 37°C. This step resulted in internalization of beads by the cell through the process of phagocytosis. The cells were then centrifuged at 150 × g for 5 min (same as during cell passaging) and resuspended in PBS to remove excess beads. They were centrifuged and resuspended once more to obtain the needed concentration (2×10^6 cells/mL) in the serum-free medium. This suspension of cells with internalized beads was then used for preparing the 2D and 3D culture samples as described above.

Spheroid morphogenesis assay in 3D on-top Matrigel culture

We followed established protocols to grow tumor-like spheroids of MCF10CA1h cells (40,41). Briefly, to create spheroids from cells seeded in the on-top configuration, first 200 μL ice-cold Matrigel (Corning, 356231) was added to a chilled 2-well imaging slide (Ibidi, 80287). Matrigel was spread evenly on the bottom of the glass using the pipette tip. The imaging slide was placed in the incubator for 30 min for the Matrigel layer to solidify. Cells were detached from the T25 flask as described above and suspended in fresh assay medium. Assay medium is the low-serum version of the complete medium, containing only 2% horse serum, while all the other ingredients are the same. Cells in suspension were mixed thoroughly with a pipette to ensure single-cell suspension. Cell concentration was estimated using a hemocytometer, and 20,000 cells were added to the 500 μL fresh assay medium. This cell solution was slowly and evenly pipetted into the 2-well slide on top of the solid Matrigel bed. The imaging slide was placed in the incubator for 30 min, during which the cells settled on top of the Matrigel layer. Next, another 500 μL assay medium containing 10% Matrigel was added on top to create final concentration of 5% Matrigel in the well. Cells formed in colonies over several days. Every 2 days, the medium in the well was carefully aspirated and replaced with fresh 5% Matrigel containing assay medium.

Brillouin microscopy

Brillouin microscopy is a spectroscopic technique that measures the inelastic scattering of light from thermal density fluctuations inside the material (spontaneous Brillouin scattering) (31,42,43). The scattered light undergoes a characteristic frequency shift when it scatters from these thermal phonons, and this frequency shift depends on the index of refraction n, mass density ρ, and the longitudinal elastic modulus M' of the probed material:

$$\nu_B = \frac{2n}{\lambda}\sqrt{\frac{M'}{\rho}}\sin\left(\frac{\theta}{2}\right),$$

where ν_B is the measured Brillouin shift and θ is the scattering angle an experimental constant (180° in our experimental setup). Longitudinal modulus M′ is the elastic constant defined as the constant that relates the uniaxial stress and uniaxial strain during compression. Therefore, Brillouin shift is an all-optical and high-resolution measurement of local mechanical properties of a given material (31). Following the current practice, in this study, we report the value of Brillouin shift in GHz as an indication of the mechanical properties of live cells, with the assumption that the $\frac{n}{\sqrt{\rho}}$ factor does not vary significantly in biological materials (44–46).

Brillouin imaging

Brillouin microscopy of cells was performed as described before (32,44). We used 60×, 0.7 NA objective (Olympus LUCPLFLN60X, Olympus, Shinjuku, Tokyo) to illuminate the sample with a light from a 660 nm laser (20–30 mW). The backscattered light was coupled into a single mode fiber and analyzed using the two VIPA cross-axis spectrometer with additional spectral purification elements (apodization and coronography (32)). Each pixel in the Brillouin images comes from one acquired Brillouin spectrum (Fig. 1 *A*). In the VIPA spectrometer, the frequencies of the light are separated in space and imaged on a high-sensitivity EMCCD camera (Andor iXon 897, Oxford Instruments, Oxfordshire, UK). Stray light from elastic scattering was blocked using adjustable slits in the spectrometer. The region that contains the anti-Stokes Brillouin scattering peak and the Stokes peak

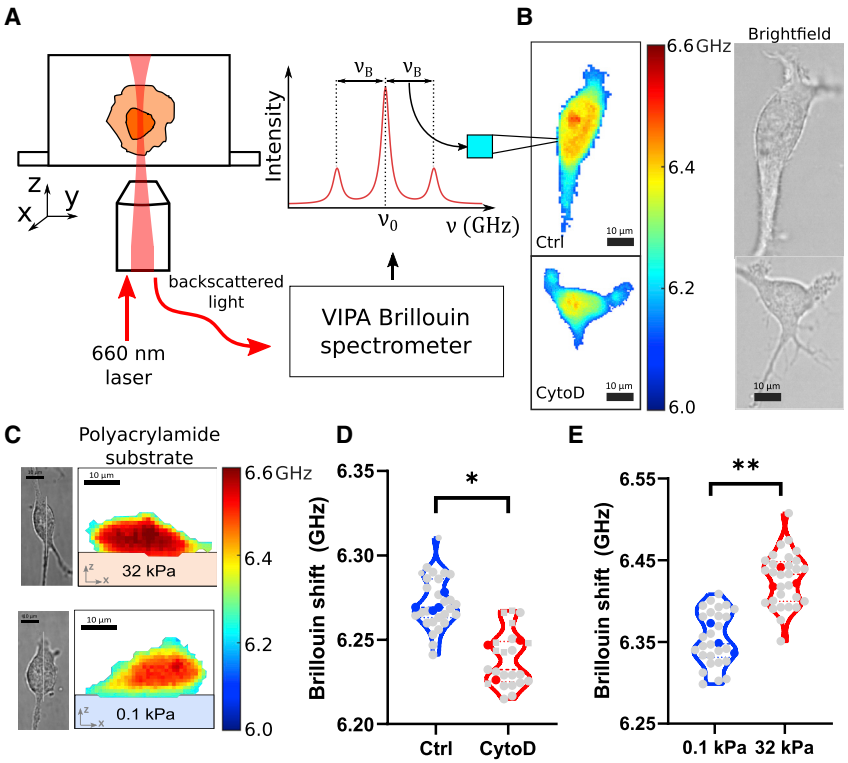

FIGURE 1 (*A*) Schematic of the experimental setup. Cells are prepared in an in vitro microenvironment (2D or 3D). Cells are illuminated with a 660 nm laser, and backscattered light from the confocal volume is analyzed using the VIPA Brillouin spectrometer. For each pixel of the image, the spectrum is analyzed, and Brillouin frequency shift is recorded. (*B*) Brillouin shift maps and bright-field images of live U87 cells: control and treated with cytochalasin D. Images represent a horizontal *x*-*y* confocal slice. Right panels are bright-field images of the same cells. (*C*). Brillouin shift maps and bright-field images of live U87 cells cultured on polyacrylamide gels of 0.1 kPa and 32 kPa stiffness. Images represent the vertical *x*-*z* confocal slice of the cell, whose location is denoted by the white line in the bright-field images. (*D*) Average Brillouin shift of cells treated with cytochalasin D (*red*) with respect to the control (*blue*) in three independent experiments. Each gray point represents average shift of all pixels in one cell, and each color point is the average all cells in one experiment. (*E*) Average Brillouin shift of cells cultured on top of polyacrylamide gels of different stiffness in the same plot as in (*D*). Unpaired *t*-test was performed on the average values of three independent experiments.

of the next diffraction order was collected. Five pixels were averaged in the direction perpendicular to the spectral dispersion axis to obtain the intensity versus frequency (in pixels) graph that contains the two Brillouin peaks (Anti-Stokes and Stokes of next diffraction order). Each of the two peaks was fitted with a Lorentzian function in a custom MATLAB program using nonlinear least squares fitting to localize peak centers. The distance between two peaks was calculated and used in further analysis to remove effects of laser frequency drift throughout the experiment. To calibrate the spectrometer, we measured the average of 500 Brillouin spectra of water and methanol collected with an exposure time of 10 ms. By using the known literature values of Brillouin shift of water and methanol, the spectral dispersion parameter (GHz per pixel) and the effective free spectral range of the spectrometer were calculated. Calibration was performed at least once an hour and after each experimental condition. Exposure time (pixel dwell time) used in cell imaging was in the range 20–50 ms, depending on the imaging depth. Typically, each measurement has shift precision of approximately 8 MHz (0.13%). Samples were placed on a 3D motorized stage and scanned across the stationary laser focus. For each imaged cell, we mapped Brillouin shift in a single horizontal or vertical plane passing through the middle of the cell.

Brillouin image analysis protocol

The culture media and Matrigel show a lower shift than cells. We identified the cell in Brillouin maps by separating it from the shift of the culture media. We did this by manually selecting a set of pixels containing the surrounding medium and keeping only pixels that at least three standard deviations larger than the average value of Brillouin shift of the medium. However, for conditions where cells are cultured on polyacrylamide gels and in gels with fibronectin-coated nanoparticle fibrils, the boundary between the cell and the polyacrylamide gels or fibrils was manually selected in the Brillouin shift maps using the imfreehand function in MATLAB. In these cases, a vertical slice is always mapped through the cell to differentiate the gel and the fibrils in the Brillouin images. Cells cultured on top of polyacrylamide gels were imaged inside a microscope stage incubation chamber at 37°C, 5% CO_2. The rest of the cells were imaged at room temperature conditions. Measurement of each sample was done within 1 h of taking the cells out of the incubator.

In the case of measuring suspended cells, we added suspended cells to the glass-bottom imaging dish immediately after harvesting from a T25 flask. We allowed 2–3 min for the cells to settle down on the glass bottom of the imaging dish. We then imaged large horizontal regions (∼150 by 150 μm) that include many cells. All measurements were performed within 20 min of adding cells to the dish, before cell attachment occurs (47). We confirmed that within this time, cell height does not change significantly by imaging vertical xz Brillouin shift slices through cells. To speed up the imaging process, we also sampled the images with a larger 2 μm step size. Cells were identified in these Brillouin shift images by thresholding at a fixed threshold of 6.15 GHz (approximately $>3\sigma$ from the value of Brillouin shift of the medium). Images were further transformed using watershed transform to separate cells from the background and to split isolated objects into individual cells (Fig. 4 *A*). This automated image processing allowed a higher throughput measurement with around 60 suspended cells per dish.

In the case of Brillouin imaging of spheroids, one horizontal slice was mapped approximately through the middle of the spheroid. Individual cell masks were manually selected in each Brillouin image (Fig. 4 *D*) in MATLAB. The centroid of each selected cell region was recorded, as well as the average Brillouin shift in that region. We quantified the mechanical variability of cells within a spheroid as a standard deviation of the Brillouin shifts of all selected cells within a spheroid. For each spheroid measured, we also calculated the Brillouin shift difference between each pair of cells. To create the plot in Fig. 4 *F*, we plotted those differences as a function of the distance between cell centroid locations in the Brillouin images.

Optical tweezer-based active microrheology

Optical tweezer experiments were performed on the experimental setup as described previously (33,34). Briefly, the experimental setup consists of a

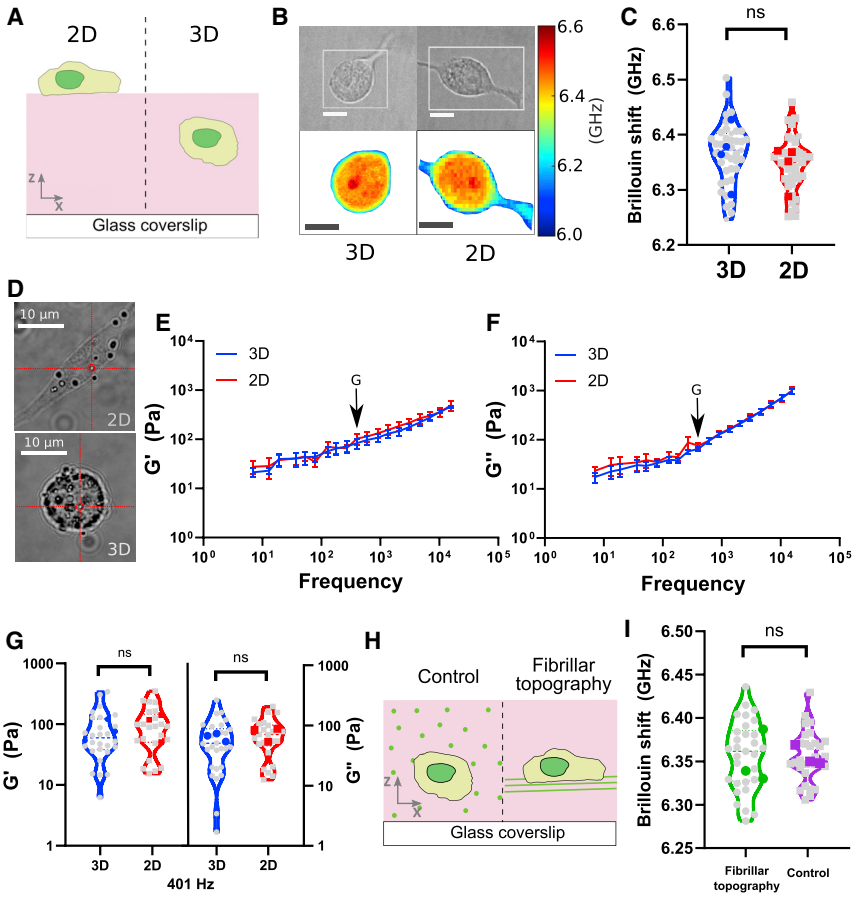

FIGURE 2 (*A*) Illustration of the two geometries in which we cultured U87 cells: on top of bulk Matrigel (2D) and inside bulk Matrigel (3D). (*B*) Example confocal Brillouin maps of cells in 2D and 3D configurations. Top images are bright-field images. The white rectangles indicate the location of the *x-y* confocal slices in which Brillouin shift was mapped. (*C*) Brillouin shift of cells grown in 2D versus 3D conditions. Unpaired *t*-test was performed on the average values of independent experiments (*color points*). (*D*) Example bright-field images of U87 cells with internalized 1 μm diameter polystyrene beads used in the optical trap measurements in 2D and 3D. (*E*) Elastic component (G') of the shear modulus measured by the optical trap as a function of frequency ranging from 7 Hz to 15 kHz of cells in 3D (*blue*) and 2D (*red*). The error bar is standard error of the mean of three independent experiments. (*F*) Viscous component (G'') of the shear modulus measured by the optical trap as a function of frequency ranging from 7 Hz to 15 kHz of cells in 3D (*blue*) and 2D (*red*). (*G*) Example shear modulus (G') and loss modulus (G'') at a single frequency denoted by arrows in (*D*) and (*F*). Each gray point is average of all the beads probed inside a single cell. Each color point is the average of an independent experiment. Two-way ANOVA was used to compare the 2D and 3D average values for G' and G'' across three independent experiments and all frequencies. (*H*) Illustration of the fibrillar topography experiment in which we cultured U87 cells in presence of the fibrillar topography (FT) and in the presence of homogeneously dispersed fibronectin-coated magnetic beads (FT control). (*I*) Brillouin shift of cells grown in FT and FT control conditions. Unpaired *t*-test was performed on the average values of independent experiments (*color points*).

detection part (detection laser 975 nm and quadrant photodetector [QPD]) and a trapping part (trapping laser 1064 nm, 100 mW power; 2D acousto-optic deflector; piezoelectric translation stage).

Sample measurement

The condenser of the microscope was placed in the Kohler illumination and the sample was put in focus. The bead of interest is positioned precisely in the center of the optical trap. This is achieved by optically scanning across the bead in 3 directions (*x*, *y*, and *z*) using a piezo XYZ nano-positioning stage (Prior, Rockland, MA, USA, 77011201) and recording the voltages on the detection path QPD. The specific relation, between voltage and nm-position β, was measured in situ by fitting the central linear region of the detector response to bead position. This allows for precise localization of the bead during trap oscillation, as previously described (34). To perform active microrheology measurements on the correctly positioned bead, the trap beam is oscillated while recording both the optical trap QPD signal (force) and the detection QPD signal (position). The oscillation of the trap beam is multiplexed as a superposition of sine waves of differing phase and frequency with the same amplitude (25.4 nm). Twenty frequencies are deliberately chosen as co-prime numbers in the range of 3 Hz to 15 kHz to avoid interference and to allow for multiplexed measurement at each frequency. We used frequencies from 7 Hz to 15 kHz in our analysis, and we removed the first frequency data point of 3 Hz due to the noise that comes from mechanical vibrations in the laboratory environment that could not be perfectly removed. The waveform is pulsed for 2 s, followed by 2 s with the trap stationary. and the sequence is repeated 7 times. Before collecting the active microrheology measurement, a 10 s passive bead spectrum is recorded. Instrument control and data acquisition are performed using custom programs (National Instruments, South Portland, ME, USA, LabVIEW).

Estimation of the local complex shear elastic modulus

Before measuring the viscoelastic constant at the location of each bead, the optical trap stiffness is calibrated in situ based on the combination of the passive and active power spectra of the bead position (48,49). Viscoelastic response of the material in the linear regime at the bead location is modeled by a generalized Langevin equation with additional terms: a harmonic term for the applied optical trap force and memory terms for viscoelastic friction $\gamma_{1,U}$ and hydrodynamic memory effects $\gamma_{2,U}$ (49–52). The equation of motion of an undriven bead is given by

$$m\ddot{x}_U(t) = F_{random}(t) - kx_U(t) - \int_0^\infty \gamma_{1,U}(\tau)\dot{x}_U(t-\tau)d\tau - \int_0^\infty \gamma_{2,U}(\tau)\ddot{x}_U(t-\tau)d\tau,$$

where, $x_U(t)$, $\dot{x}_U(t)$, and $\ddot{x}_U(t)$ are the undriven bead position, velocity, and acceleration, respectively; t is time, τ is correlation time, $F_{random}(t)$ is the

Langevin noise term, k is the stiffness of the optical trap, m is the mass of the trapped bead, and $\gamma_{1,U}(\tau)$ and $\gamma_{2,U}(\tau)$ are the time-dependent memory functions representing friction and hydrodynamic memory effects, respectively. The equation of motion for a bead driven by moving the position $x_L(t)$ of the laser is given by

$$m\ddot{x}_U(t) = F_{random}(t) - k(x_D(t) - x_L(t)) - \int_0^\infty \gamma_{1,D}(\tau)\dot{x}_D(t-\tau)d\tau - \int_0^\infty \gamma_{2,D}(\tau)\ddot{x}_D(t-\tau)d\tau,$$

where $x_D(t)$, $\dot{x}_D(t)$, and $\ddot{x}_D(t)$ the driven bead position, velocity, and acceleration respectively, and $\gamma_{1,D}(\tau)$ and $\gamma_{2,D}(\tau)$ are the time-dependent memory functions representing friction and hydrodynamic memory effects, respectively, in the driven case. Onsager's regression hypothesis, which is a consequence of the fluctuation-dissipation theorem, allows us to assume that the friction relaxation spectrum is equal in the driven and undriven system $\gamma_{1,U}(\tau) = \gamma_{1,D}(\tau)$ and $\gamma_{2,U}(\tau) = \gamma_{2,D}(\tau)$ (48–52). This is valid in the case when the driven motion of the bead is on the same scale as the passive motion of the bead due to the Brownian motion. The spectrum of the actively driven bead is defined as $R_L(\omega) \equiv \frac{\tilde{x}_{dr}(\omega)}{-i\omega\tilde{x}_L(\omega)}$, where $\tilde{x}_{dr}(\omega)$ and $\tilde{x}_L(\omega)$ are the Fourier transforms of the positions as a function of time of the trapped bead and the trapping laser, respectively, that are recorded while the trap is oscillating. The active driven spectrum $R_L(\omega)$ can be used to estimate the friction relaxation function $\gamma_D(\omega) \equiv \tilde{\gamma}_{1,D}(\omega) + i\omega\tilde{\gamma}_{2,D}(\omega)$ according to the following equation:

$$\gamma D(\omega) + i\omega m = \frac{k}{i\omega}\left(\frac{1}{i\omega R_L(\omega)} + 1\right),$$

where ω is the trap oscillation frequency in rad/s and ∼ indicates Fourier transform. The optical trap stiffness can be determined from the real part of the active power spectrum and the passive power spectrum and is given by $k = \frac{Re\{R_L(\omega)\}}{P_U(\omega)}$, where $P_U(\omega) = \langle|x_U(\omega)|^2\rangle$ and $\tilde{x}_U(\omega)$ is the Fourier transform of the position of the undriven bead as a function of time while the trapping laser is stationary. The friction relaxation spectrum $\gamma_D(\omega)$ is related to the complex viscoelastic modulus of the surrounding microenvironment by the generalized Stokes-Einstein relation $G^*(\omega) = \frac{i\omega\gamma_D(\omega)}{6\pi a}$, where m is bead mass and a is the hydrodynamic radius of the bead. The complex viscoelastic modulus can be written as

$$G^*(\omega) = |G^*|e^{i\delta} = G' + iG'',$$

where $|G^*| = (G'^2 + G''^2)^{1/2}$ is the magnitude and δ is the loss tangent $tan(\delta) = G''/G'$, and they encode rigidity and hysteresivity, respectively. The real part G' represents the storage (elastic) modulus, and the imaginary part G'' represents the loss (viscous) modulus.

Data analysis and statistics

For each cell analyzed, 3–5 beads were measured at different locations within the cell. Only cells exceeding ∼30 μm from the coverslip were analyzed in accordance with Faxen's law. Between 7 and 10 cells were analyzed per sample in each experiment, and three independent experiments were performed (for three independent samples fabricated across different days and across different cell passage numbers). Data were analyzed using custom MATLAB and GraphPad Prism programs.

The measurements of the modulus magnitudes $|G^*(\omega)|$, G', and G'' for each single bead are distributed according to the log-normal distribution. The mean value of these magnitudes from the repeated measurements on the same bead are calculated using the maximum-likelihood estimate for the mean of the log-normal distribution (33).

$$\mu = exp\left[\frac{1}{n}\sum_{i=1}^{n}\ln(x_i) + \frac{1}{2}\left[\frac{1}{n-1}\sum_{j=1}^{n}\left|\ln(x_j) - \frac{1}{n}\sum_{i=1}^{n}\ln(x_i)\right|^2\right]\right]$$

The maximum-likelihood estimate of the log-transformed variance is given by

$$\sigma^2 = \mu^2\left[exp\left[\frac{1}{n-1}\sum_{j=1}^{n}\left|\ln(x_j) - \frac{1}{n}\sum_{i=1}^{n}\ln(x_i)\right|^2\right]\right].$$

In case of the loss tangent, which is normally distributed, we use arithmetic mean and standard deviation as estimates of central tendency and dispersion among measurements.

We assume beads measurements within each cell and cells within the cell population are normally distributed. Active microrheology data are presented as mean complex, storage, or loss moduli versus frequency from 7 Hz to 15 kHz of all beads in a single cell. Average values of the G′ and G″ for all cells in one dish (one experiment) were collected from three independent experiments. These (n = 3) values were compared across all frequencies, and the presence of statistically detectable differences was analyzed with a two-way ANOVA test with Tukey's post hoc correction.

Cell shape analysis

Bright-field images of each cell sampled by Brillouin microscope was used to identify cell shape. Cell shape was detected using a custom-built MATLAB semi-automatic cell detection GUI program. Each image intensity was normalized, and images were sent through an edge detection protocol (53) that created a binary gradient mask based on the Sobel algorithm. This binary image was dilated to connect edges, holes were filled, and the binary image was eroded (to undo the dilation while preserving the large objects—cells). Each detected preliminary cell shape was inspected and manually edited to select the correct cell region in the field of view using MATLAB's imfreehand function. The edge detection protocol depends on the contrast of the bright-field images, and it is not always perfectly accurate, especially when there are multiple objects in the image in addition to the cell, e.g., aligned fibrils. For this reason, we manually inspected and corrected each image. Binary images of cells were analyzed in MATLAB to extract the relevant shape parameters: area, major and minor axis of fitted ellipse, and perimeter. We quantified the aspect ratio as the ratio of minor to major axis of the fitted ellipse and circularity as perimeter^2/(4π × area).

RESULTS

Brillouin shift correlates with modulation of cell mechanics in cells cultured on 2D substrates

The actin cytoskeleton has been shown to be a key regulator of the mechanical properties of cells. We first assessed the Brillouin shift of cancer cells cultured in 2D in the presence and absence of cytochalasin D, a pharmacological inhibitor of actin (44,54–57). We determined that the average Brillouin shift of cancer cells decreases by 30 MHz (Fig. 1 *A* and *C*) when treated with 1 μM cytochalasin D for 30 min. Cells can modulate their internal mechanical properties, morphology, and organization of the cytoskeleton in response to substrate stiffness (58–60). We next asked if

there are differences in Brillouin shifts for cells cultured on different substrate stiffnesses. We determined that there is a distinct difference in Brillouin shift for cells grown on soft versus stiff substrates. Cells cultured on hard (32 kPa) polyacrylamide gels adopted a Brillouin shift 75 MHz higher than cells cultured on soft polyacrylamide gels (0.1 kPa). We calculated the average Brillouin shift of a whole cell (Fig. 1 *D* and *E*, *gray points*) and used those to estimate the mean Brillouin shift of cells in each condition (Fig. 1 *D* and *E*, *color points*, one for each independent experiment).

Cells cultured on top of hydrogels and embedded in hydrogel share similar mechanical phenotype

The effects of substrates with different properties (e.g., stiffness or ligand density (61)) on cell have been extensively studied. However, the effects of distance and boundary conditions on cells' ability to sense a physical cue such as substrate stiffness is less understood. Specifically, if a cell is plated on top of a soft flat hydrogel (∼100 Pa) of a given thickness on a glass dish surface (>GPa), do cells behave comparably to a boundary condition where the soft substrate is infinite and isotropic in every direction (Fig. 2 *A*)? In other words, what is the boundary condition that governs mechanical phenotype of cells? We take advantage of the ability of Brillouin microscopy to noninvasively map mechanical properties of cells in 3D to address this question. We measured live cells embedded in 3D laminin-rich hydrogel (Matrigel) and compared them with the cells grown on top of a flat hydrogel of the same composition (Fig. 2 *A–C*). Cell morphological analysis using bright-field images revealed a diversity of shapes where some cancer cells in 3D were spherical and some adopted elongated shapes. Comparative analysis for cells grown on a 2D laminin-rich extracellular matrix (ECM) hydrogel shows the characteristic elongated and flat morphology. Even though cells respond differently to 3D and 2D configurations, we consistently find no difference in Brillouin shift of cells in these two conditions (Fig. 2 *A–D*).

To independently investigate the mechanics of cells in these two configurations, we performed the same experiments using high-frequency optical tweezer microrheology. This technique can probe complex elastic modulus of live cells directly in three dimensions by actively driving 1 μm beads embedded in the cell cytoplasm across frequencies ranging from 7 Hz to 15 kHz (33,34) (see materials and methods.) We again determined that the complex elastic modulus of cells cultured in 3D and 2D configurations were comparable across all measured frequencies. The measured shear modulus at 19 Hz was $G'_{(3D)} = 39 \pm 11$ Pa and loss modulus $G''_{(3D)} = 25 \pm 7$ Pa (Fig. 2 *E* and *F*).

Fibrillar structures are present in vivo and alter cancer cell migration (62). Cells can sense the FT in their environment independently of the adhesion ligands that the fibrils present to the cell (37). Using Brillouin microscopy, we set out to investigate whether cells also alter their mechanics in the presence of the FT in 3D. Here, we used a model previously developed in our lab to fabricate fibrillar architecture in 3D (37–39). We used magnetic nanoparticles coated with human fibronectin that, in the presence of a magnetic field, align into 1–2 μm-thick fibrils that are embedded in the 3D hydrogel (Matrigel) together with cells. We previously determined that the overall mechanical and diffusive properties of the hydrogel were not altered due to the presence of the aligned particles. Instead, the presence or absence of cell protrusions were dictated by the aligned fibrils (37) (Fig. 2 *G* and *F*). As mechanical phenotypes of cells are responsive to tissue anisotropy, we next asked if the mechanical phenotype is also altered. We determined that the mechanical phenotype of cells cultured in presence of fibrillar architecture and control conditions was similar as that measured by quantifying the Brillouin shift.

Cell mechanical state is a variable parameter that correlates to cell morphology

Within a given sample, cells adopt morphogenetic heterogeneities (36,63). We next asked if we can further identify subtypes of mechanical phenotypes based on classification of different morphologies. First, we used the bright-field images of all cells, which we imaged with Brillouin microscopy to determine cell morphology. To remove the underlying variability in mechanical properties of cell subpopulations in the data, we devised a classification scheme based on the circularity and aspect ratio of cell shapes. Circularity is defined as the ratio of the shape area and the square of its perimeter. It is normalized in such a way to be in the range between 0 and 1, where perfect circle has circularity of 1. Similarly, the aspect ratio is a measure of deviation from the perfectly round morphology. Here, we define the aspect ratio as the ratio of minor to major axis of the fitted ellipse to the shape boundary. This ensures that the aspect ratio also falls in the range from 0 to 1. By combining these two parameters, we can identify cells that either have comparable values of aspect ratio and circularity or cells that have low circularity but an intermediate or high value of aspect ratio. Within the first subset of cells that have comparable circularity and aspect ratio, we further divide those into two groups: round cells and elongated but not protrusive (type A: round cells aspect ratio (AR) $>$ 0.75, and type B: elongated cells AR $<$ 0.75). The remaining subset of shapes with very low circularity for the given aspect ratio (circularity: AR $>$ 0.2) revealed cells of very long perimeter, which indicated morphologies with an abundance of protrusions (type C).

Using this classification, we identified detectable differences in Brillouin shift among these three shape types (Fig. 3 *C*). We then focused on one morphological classification and asked if culture conditions then determined the

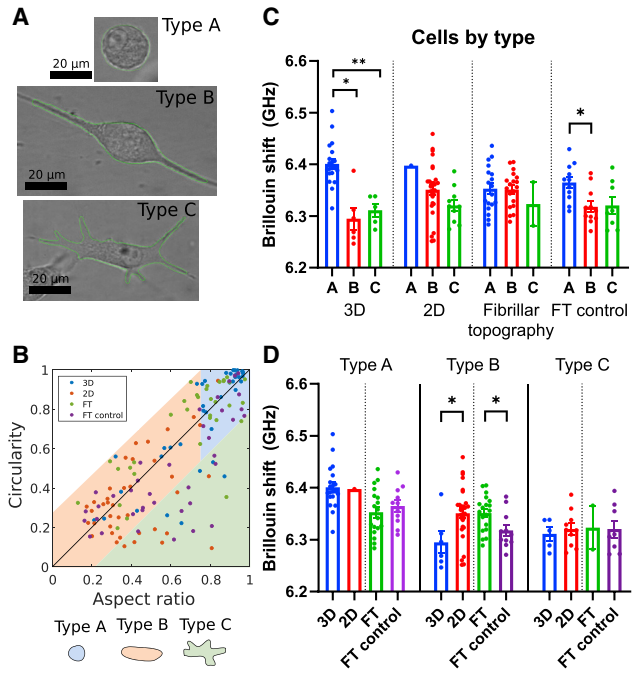

FIGURE 3 (*A*) Example bright-field images of U87 cells and the shape outlines (*green line*) (*B*) Scatter plot of circularity versus aspect ratio (minor/major axis) of all cells. Cells were classified by type according to the region of the scatter plot in which they fall. Type C (irregular) cells are defined as cells that are more than two standard deviations away from the identity line. The rest of the cells are classified as type A and type B cells. Type A (round) cells are identified as cells that have an aspect ratio larger than 0.75 (3/4). Type B cells (elongated) have an aspect ratio less than 0.75 (3/4). (*C*) Plot of average Brillouin shift of cells measured in the four conditions described in Fig. 2., separated by cell type. Within some conditions, there are differences in Brillouin shift of cells of different types. (*D*) Comparison of 3D versus 2D and aligned versus non-aligned Brillouin shift of all cells within a single-cell morphology type. In type B group, Brillouin shift of 3D cells is lower than the Brillouin shift of 2D cells, while cells grown in presence of FT have higher shift than the cells grown in an isotropic matrix (FT control). Unpaired *t*-test for comparing 3D versus 2D and FT versus FT control conditions in each category with at least three cells.

Brillouin shift. We determined that the type B cells—elongated but not protrusive—adopted a higher Brillouin shift when cultured in a 2D environment than when cultured in 3D (0.0559 ± 0.023 GHz). Moreover, cells of the same type B also adopted a higher shift in the presence of the FT than in the homogeneous 3D environment (-0.0333 ± 0.0131 GHz). In case of the optical trap microrheology, beads inside the cell at high numbers can affect the physiology of cells, and thus there were not enough measurements of cells in each morphology type to make a similar comparison.

Cell mechanical properties in multicellular systems

To investigate cell mechanical properties in the context of 3D culture that includes cell-cell interactions, we turn to the in vitro method of 3D culture of breast epithelial cell spheroids. This method is well established and allows for repeatable formation of mammary gland-like spheroids using laminin-rich ECM (Matrigel). Here, we employed the MCF10CA1h (M3), a human breast cancer line. This cell line forms robust spheroids when cultured in laminin-rich ECM using the "3D on-top" method (40,41). Using Brillouin microscopy, we mapped the mechanical properties of individual cells in suspension and longitudinally from day 0 to 5 during growth of spheroids. To investigate the mechanical state of cells, we take advantage of the high-resolution nature of Brillouin microscopy to identify single cells in the Brillouin maps (Fig. 4 *E*). By manually selecting each cell in each image, we can estimate the Brillouin shift of only the cells within the spheroid and thus remove effects of differential cell packing or any cell-free spaces inside the spheroid. We find that the heterogeneity of Brillouin shifts is smaller in spheroids when compared with single cells. The heterogeneity among spheroids is the same as the heterogeneity of single cells within those spheroids. To check if the mechanical similarity between cells is stronger between neighboring cells versus cells at the distant parts of the spheroid, we looked at the differences in Brillouin shift between each cell pair within a given spheroid. Plotting this data for all day 5 spheroids of M1 cells, we find that the average Brillouin shift difference for a pair of cells in a spheroid is a constant function of pairwise distance between cells (Fig. 4 *F*).

DISCUSSION

Cancer cells exhibit distinct mechanical properties compared with those measured for the normal counterparts that are context dependent (2,28,64,65). One promising idea is to use mechanical phenotype to predict metastatic potential and drug responsiveness in order to aid diagnosis and treatment. However, the measured mechanical properties are determined by environmental factors such as availability and chemical identity of ligands (66), nearest neighbor interactions with cells (23), and ECM components (67). In addition, the measured values of the cellular mechanical properties depend on the length and temporal scales at which the measurements are performed (26,33,68). Thus, what is needed is the ability to measure mechanical properties of cells within native tissue microenvironments. Here, we employed a noncontact, label-free technique, Brillouin microscopy, to probe modulation of mechanical properties of cells in complex microenvironments. Furthermore, we employed broadband frequency range optical tweezers to probe the microrheology of cells to provide complementary μm-scale measurements to validate our Brillouin microscopy results in a 3D complex in vitro system. We applied these techniques to established in vitro models that recapitulate in vivo basement membrane stoichiometry and tissue anisotropy. We find good agreement between two

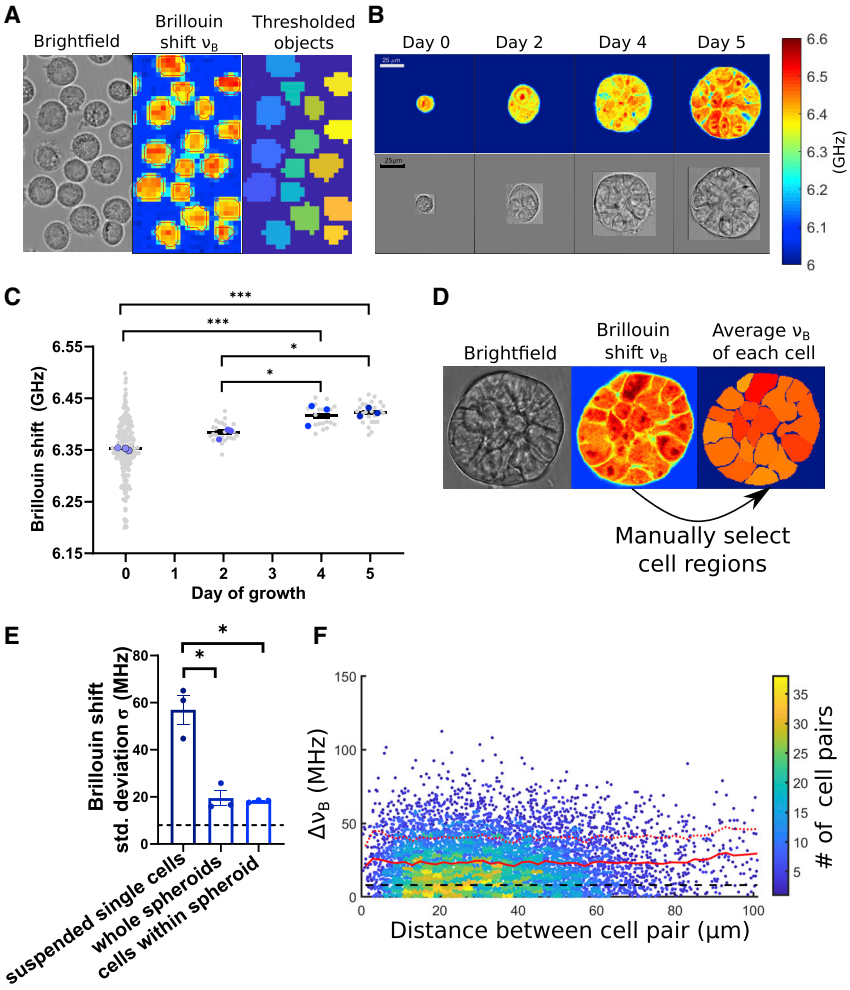

FIGURE 4 (*A*) Example Brillouin image and corresponding bright-field image of suspended cells in a dish. Individual cells were identified in the Brillouin shift images by thresholding and watershed transform (see materials and methods). (*B*). Example Brillouin shift maps of cells and spheroids at different stages of growth. (*C*) Average Brillouin shift of cells and whole spheroids (*gray points*) in three independent experiments (*color points*). Each experiment is average of multiple spheroids (n = 7 ± 2 spheroids) and in case of suspended cells (day 0) (n = 58 ± 3 cells). Statistical difference was detected using one-way ANOVA with Tukey's correction performed on the average values of the three independent experiments (n = 3). (*D*) Illustration of the process of identifying single cells within the spheroid. Single cells are manually selected in the Brillouin shift maps, and the shift in each cell is averaged. (*E*) Standard deviation of measured Brillouin shifts of cells in three cases: across all single cells measured in an independent experiment (n = 58 ± 3 cells), across all spheroids in an independent experiment (n = 7 ± 2 spheroids), and across cells within a single spheroid (averaged over all spheroids in given experiment (n = 17 ± 6 cells, $n_{spheroids}$ = 7 ± 2). (*F*) Absolute difference in Brillouin shift versus cell distance for all pairs of cells within single spheroids, across all day 5 spheroids of MCF10CA1h cells (n_{pairs} = 7,266, Pearson correlation coefficient ρ = 0.025). Color of scatter plot denotes the density of points. Distances were binned in the bins of size 2 μm and average shift (*solid red line*) and 1σ error (*dashed red line*) as a function of cell pair distance are plotted. Shift values at distances >60 μm were smoothed with a 5 bin moving average to remove the noise due to a small number of pairs in those bins.

independent methods, optical trap and Brillouin microscopy, for probing single-cell mechanics. Here, we demonstrated that live-cell Brillouin microscopy revealed shifts that are sensitive to environmental conditions and pharmacological perturbations. We also longitudinally mapped mechanical changes as a function of spheroid formation from single-cell to multicellular structures. We show that this technique is sensitive to heterogeneities that arise due to nearest neighbor effects and due to differences in cell morphology.

Mechanical phenotyping of tissues at multiple length scales have been of great interest in the field of mechanobiology. Optical-based techniques such as optical stretchers (69), optical and magnetic tweezer-based modalities (33,70,71), and real-time deformation cytometry (72) have been employed to probe μm-scale mechanical phenotypes. However, many of these techniques for assessing material properties are unable to probe microscale mechanics for cells embedded in complex 3D tissues. We and others recently employed optical tweezer-based active microrheology to map microscale mechanical properties in 3D culture models and in a living animal (33,73–75). Several technological advancements such as the in situ trap stiffness calibration and high-sensitivity localization of the probe bead have enabled the applications in 3D cultures and in living animals (34). Additionally, broadband frequency analysis allows quantitation of distinct viscoelastic profile such as individual cell stiffnesses and hysteresivity or relative liquid- or solid-like behavior. Access to the higher frequencies also can be used to probe additional rheological metrics such as a power law dependence in different materials. However, this and similar methods are limited to the use of introduced probes, such as polystyrene beads, or intrinsic components, such as organelles, to infer the underlying mechanical properties. In the case where external probes are introduced into tissue, these probes must be introduced in numbers and densities that do not compromise cellular integrity and function. This can then result in under sampling of the cell interior at the level of single cells for some tissues. In the latter case, the intrinsic organelles may be of different sizes and shapes, which makes it difficult to translate underlying deformation of tissue to a rheological value. Moreover, the application of

forces to these organelles may drive an unwanted perturbation in physiological function. Thus, a purely noninvasive method to map the mechanical properties of tissue with high resolution is desirable. Brillouin microscopy is an all-optical and purely noninvasive method. Thus, it provides an attractive and complementary approach to address this need.

Brillouin shift is a measure of the longitudinal elastic modulus, if we know the index of refraction and mass density of the material. In typical biological materials such as cells or tissues, these parameters are not always known or directly measurable, and for that reason, this and majority of other studies report values of Brillouin shift in GHz rather than the value of the longitudinal modulus. Interestingly, for most cells and tissues, the ratio of the refractive index and the square root of the density remains constant, since both index of refraction and density vary together, and the dominant contribution to Brillouin shift comes from the changes in M'. Therefore, Brillouin shift is used as a measurement proportional to square root of the local longitudinal elastic modulus at high frequency (44–46). In most cells and tissues, this assumption is valid, but there are exceptions, like lipid-rich samples, where the mass density and index of refraction have dramatically different values (76,77).

It is important to comment on the meaning of Brillouin measurements as mechanical testing method in order to capture the biomechanical origin of the measured cellular changes. Brillouin scattering probes the longitudinal modulus on the GHz timescale (43), a fundamentally different quantity from the traditionally measured Young's and shear moduli at quasi-static frequencies. Therefore, there is a dramatic timescale difference between these measurements. One on hand, there is difference in the moduli that is measured. The definition of the moduli is distinct as Young's and shear do not involve volume changes in the sample, while the longitudinal modulus involves a uniaxial deformation due to uniaxial stress (43). Because of these differences, there is not a theoretically established correlation between these moduli for biological soft matter. Nevertheless, we and others have previously shown empirically a widespread series of relationships between changes in the Brillouin shift and changes in the stiffness obtained using traditional rheological methods in cells and tissues. Such empirical correlations are probably due to a common dependence of longitudinal and Young's/shear moduli to underlying structural and biophysical factors within samples (44,45,78). The findings of this paper are consistent with this interpretation: both Brillouin and Young's/shear moduli are expected to increase with cytoskeletal changes such as actin upregulation, cross-linking, or branching as well as with an increased relative contribution of the stiffer nucleus. In this respect, the multimodal analysis is important because of the spatio-temporal scale characteristics of Brillouin scattering and optical traps (79,80). However, there are two important differences between these methods. They measure different rheological parameters (shear versus longitudinal moduli), and they probe the mechanical properties at different timescales (Hz-kHz versus GHz). The observed good agreement of microscale properties between the two modalities at different timescales points to the fact that the underlying material structure of the live cell can be probed in different rheological experiments and that a cell's mechanical phenotype determined in such a way can be used as a biomarker of the overall cell state.

Cells adopt different morphologies in different tissue environments (36,81). It has been postulated that cell morphology is linked to cell fate and may also be linked to predicting metastatic potential (63). These studies have implicated physical traits such as cell morphology, mechanical phenotype, and migration as determinants of aggressiveness of many types of cancers such as breast, pancreatic, osteosarcomas, and prostate cancers (82–84). These studies have also performed combinatorial morphometrics and transcriptomics in efforts to yield predictions of metastasis (59,63,85). Differences in cell morphology point to the differences of overall cell state, which may also reflect differences in mechanical properties (20,44,64,86). Hence, we compared the cell mechanics as a function the environment as a function of the cell morphology. Here, we determined that for similar morphologies, cells adopt different mechanical phenotypes due to environmental conditions. Our findings support the idea that physical parameters such as the mechanical properties can also be a proxy for cell state in a context-dependent manner. However, this and other data suggest that combinatorial analysis of multiple physical parameters, such as morphology and mechanical properties, will be needed to increase predictive capacity of cell fate and function.

Nuclear mechanics is closely related to the cytoskeleton structure and mechanical state of the cytoplasm (54). In this analysis, we are comparing the values of Brillouin shift averaged across entire cells, which we use as the measurement of the mechanical state of individual cells. However, the nucleus has a higher Brillouin shift than the cytoplasm (Fig. S1 *C*; (54,87)), and the variation of the nuclear size could affect the average value of the average cell Brillouin shift. This is an important contribution for the differences for cells of type A (round cells) having a higher Brillouin shift than the cells of type B and C. (Figs. 3 *C* and S1 *B*). The variation of nuclear sizes in U87 cells cultured in soft hydrogel conditions corresponds to a variation in Brillouin shift on the order of 50 MHz, which is comparable to the changes we detect across our conditions, but in some cases, we observe Brillouin shift differences larger than that (see supporting material). This suggests that the observed Brillouin shift changes are due to changes that go beyond only the change in proportion of nucleus measured. This underscores the additional information that spatial maps may provide with respect to just obtaining whole-cell values.

Nevertheless, if whole-cell values are of interest, these considerations justify our analysis, which includes a classification

by cell-shape type. We observed that the cells of similar elongated shape in 2D have a higher shift. This could be explained by the establishment of dorsoventral cell polarity in 2D condition where cells adhere to the ECM only along one surface, while in 3D there are different factors that regulate cell polarity (4). It has been previously postulated that in cells that are adherent on a surface, the nucleus is compressed by the cytoskeleton, and increased stress in concert with increased contractility could lead to nuclear stiffening (54,86). This speculation agrees with the fact that that the cells of type B in the presence of FT also have a higher shift than the control, since in the presence of the aligned fibrils in 3D, cells could have a preferential attachment direction. However, it was previously observed that the ECM has a higher stiffness near the fibrils (37), so the increase in Brillouin shift of cells in the presence of fibrils could also be attributed to the cells' response to the locally stiffer matrix.

Tissues are multicellular units that can be homogenous cell types or combinatorial organization of different types of cells. Organoid and 3D culture models allow the recapitulation of microtissues observed in vivo for a multitude of epithelial organs (25,41,88–91). Moreover, they can also recapitulate the progressive disordered architectures associated with the malignant transformation (67,92). Dynamic cell behaviors such as coherent rotation (93), cell-cell adhesion turnover (23), and coordinated cell-ECM interactions (5,6,94) are important in the establishment of glandular tissues and become dysregulated in the malignant transformation. However, it is less understood how cells regulate cross talk across multiple spatial and temporal scales. One idea is that there is a mechanical coupling that acts a feedback mechanism to facilitate multicellular growth. We recently determined that there is a microscale coupling between normal cells and matched organ ECM microenvironment using optical trap-based active microrheology (33). We also determined that there was a mismatch between intracellular cell mechanics with that of the surrounding matrix environment that was dependent on chemical specificity of the ECM hydrogel. This technique can be employed for longitudinal mapping of multicellular spheroids. However, in case of determination of multicellular coupling, the measurement throughput is limited, as it heavily relies on the optimized introduction of external probes in every cell within a spheroid. Here, Brillouin microscopy rapidly determined the mechanical properties of individual cells and revealed the mechanical similarity among cells during the establishment of spheroids across multiple days. For single cells in 2D and 3D, cell shape in 2D bright-field images is a good approximation of the real cell shape. On the other hand, in spheroids cells are tightly packed and take complex shapes. In confocal Brillouin slices, cell boundaries can be easily distinguished, and we take advantage of this to approximate the Brillouin shift of each cell by manually selecting them. Note that without imaging a full volume of the spheroid, which is still impractical due to limited speed of acquisition (~10–15 min per confocal slice of the spheroid), we cannot get an estimate of the complex cell shapes inside the spheroids. For this reason, we quantify the variance of average Brillouin shifts on the level of individual cells. The decreased heterogeneity among cells in spheroids points to the existence of mechanical cooperativity between cells that make up a single spheroid. We are able to detect cell-to-cell variability (~20 MHz), which is smaller than the variability of single cells (~45 MHz). Furthermore, we find that this variance is spatially constant across the spheroid, as the differences in the mechanical properties of any two cells do not depend on their distance within the spheroid. It is important to note that the cell colonies start growing from single cells, and the uniformity in mechanical properties could be explained by their clonal nature.

In summary, using all-optical methods, we quantify the mechanical properties of single cells and multicellular structures in 3D environments that were not accessible before. In 3D spheroids, we observed a lower variance of Brillouin shifts compared with single cells. In addition, we have shown that the mechanical state of the cell is dynamic and changes depending on the context. In the future, it will be interesting to investigate the relationship between the expression of key cell-cell and cell-ECM interaction proteins in the spheroids in relation to the mechanical heterogeneity of cells to elucidate the role of mechanical coupling of cells in multicellular systems.

DATA AVAILABILITY

The raw and processed data required to reproduce these findings are available from Kandice Tanner, PhD, at 37 Convent Dr., Bethesda, MD 20852, USA (kandice.tanner@nih.gov).

SUPPORTING MATERIAL

Supporting material can be found online at https://doi.org/10.1016/j.bpj.2022.09.002.

AUTHOR CONTRIBUTIONS

K.T., G.S., and M.N. designed the research. M.N. performed the research and analysis. K.T., G.S., and M.N. wrote the manuscript.

ACKNOWLEDGMENTS

We thank Dr. Woong Young So for the help with the optical tweezer setup and experiments. We also thank Dr. Colin Paul for the assistance with the 3D fibrillar architecture microenvironment engineering. This effort was supported by the Intramural Research Program of the National Institutes of Health, the National Cancer Institute, NCI-UMD Partnership for Integrative Cancer Research, National Institutes of Health (R21-CA258008), and National Science Foundation (CMMI 1929412).

DECLARATION OF INTERESTS

M.N. and G.S. are inventors of patents related to the Brillouin technology. G.S. is a consultant for Intelon Optics. K.T. declares no competing interests.

REFERENCES

1. Paul, C. D., P. Mistriotis, and K. Konstantopoulos. 2017. Cancer cell motility: lessons from migration in confined spaces. *Nat. Rev. Cancer.* 17:131–140. https://doi.org/10.1038/nrc.2016.123.
2. Gensbittel, V., M. Kräter, …, J. G. Goetz. 2021. Mechanical adaptability of tumor cells in metastasis. *Dev. Cell.* 56:164–179. https://doi.org/10.1016/j.devcel.2020.10.011.
3. Winkler, J., A. Abisoye-Ogunniyan, …, Z. Werb. 2020. Concepts of extracellular matrix remodelling in tumour progression and metastasis. *Nat. Commun.* 11:5120. https://doi.org/10.1038/s41467-020-18794-x.
4. Yamada, K. M., and M. Sixt. 2019. Mechanisms of 3D cell migration. *Nat. Rev. Mol. Cell Biol.* 20:738–752. https://doi.org/10.1038/s41580-019-0172-9.
5. Xu, R., A. Boudreau, and M. J. Bissell. 2009. Tissue architecture and function: dynamic reciprocity via extra- and intra-cellular matrices. *Cancer Metastasis Rev.* 28:167–176. https://doi.org/10.1007/s10555-008-9178-z.
6. Nelson, C. M., and M. J. Bissell. 2006. Of extracellular matrix, scaffolds, and signaling: tissue architecture regulates development, homeostasis, and cancer. *Annu. Rev. Cell Dev. Biol.* 22:287–309. https://doi.org/10.1146/annurev.cellbio.22.010305.104315.
7. Bissell, M. J., D. C. Radisky, …, O. W. Petersen. 2002. The organizing principle: microenvironmental influences in the normal and malignant breast. *Differentiation.* 70:537–546. https://doi.org/10.1046/j.1432-0436.2002.700907.x.
8. Chaudhuri, O., S. T. Koshy, …, D. J. Mooney. 2014. Extracellular matrix stiffness and composition jointly regulate the induction of malignant phenotypes in mammary epithelium. *Nat. Mater.* 13:970–978. https://doi.org/10.1038/nmat4009.
9. Hanahan, D., and R. A. Weinberg. 2000. The hallmarks of cancer. *Cell.* 100:57–70. https://doi.org/10.1016/S0092-8674(00)81683-9.
10. Bao, G., and S. Suresh. 2003. Cell and molecular mechanics of biological materials. *Nat. Mater.* 2:715–725. https://doi.org/10.1038/nmat1001.
11. Alibert, C., B. Goud, and J.-B. Manneville. 2017. Are cancer cells really softer than normal cells? *Biol. Cell.* 109:167–189. https://doi.org/10.1111/boc.201600078.
12. Wullkopf, L., A.-K. V. West, …, J. T. Erler. 2018. Cancer cells' ability to mechanically adjust to extracellular matrix stiffness correlates with their invasive potential. *Mol. Biol. Cell.* 29:2378–2385. https://doi.org/10.1091/mbc.E18-05-0319.
13. Guo, M., A. F. Pegoraro, …, D. A. Weitz. 2017. Cell volume change through water efflux impacts cell stiffness and stem cell fate. *Proc. Natl. Acad. Sci. USA.* 114:E8618. https://doi.org/10.1073/pnas.1705179114. http://www.pnas.org/content/114/41/E8618.abstract.
14. Byfield, F. J., R. K. Reen, …, K. J. Gooch. 2009. Endothelial actin and cell stiffness is modulated by substrate stiffness in 2D and 3D. *J. Biomech.* 42:1114–1119. https://doi.org/10.1016/j.jbiomech.2009.02.012. http://www.sciencedirect.com/science/article/pii/S0021929009000931.
15. Weder, G., M. C. Hendriks-Balk, …, A. Mariotti. 2014. Increased plasticity of the stiffness of melanoma cells correlates with their acquisition of metastatic properties. *Nanomed. Nanotechnol. Biol. Med.* 10:141–148.
16. Cross, S. E., Y.-S. Jin, …, J. K. Gimzewski. 2007. Nanomechanical analysis of cells from cancer patients. *Nat. Nanotechnol.* 2:780–783. https://doi.org/10.1038/nnano.2007.388.
17. Harada, T., J. Swift, …, D. E. Discher. 2014. Nuclear lamin stiffness is a barrier to 3D migration, but softness can limit survival. *J. Cell Biol.* 204:669–682. https://doi.org/10.1083/jcb.201308029.
18. Nguyen, A. V., K. D. Nyberg, …, A. C. Rowat. 2016. Stiffness of pancreatic cancer cells is associated with increased invasive potential. *Integr. Biol.* 8:1232–1245. https://doi.org/10.1039/c6ib00135a.
19. Rianna, C., M. Radmacher, and S. Kumar. 2020. Direct evidence that tumor cells soften when navigating confined spaces. *Mol. Biol. Cell.* 31:1726–1734. https://doi.org/10.1091/mbc.E19-10-0588.
20. Roberts, A. B., J. Zhang, …, G. Scarcelli. 2021. Tumor cell nuclei soften during transendothelial migration. *J. Biomech.* 121:110400.
21. Sanz-Moreno, V., G. Gadea, …, C. J. Marshall. 2008. Rac activation and inactivation control plasticity of tumor cell movement. *Cell.* 135:510–523. https://doi.org/10.1016/j.cell.2008.09.043.
22. Wolf, K., I. Mazo, …, P. Friedl. 2003. Compensation mechanism in tumor cell migration: mesenchymal-amoeboid transition after blocking of pericellular proteolysis. *J. Cell Biol.* 160:267–277. https://doi.org/10.1083/jcb.200209006.
23. Padmanaban, V., I. Krol, …, A. J. Ewald. 2019. E-cadherin is required for metastasis in multiple models of breast cancer. *Nature.* 573:439–444. https://doi.org/10.1038/s41586-019-1526-3.
24. Cheung Kevin, J., and J. Ewald Andrew. 2016. A collective route to metastasis: seeding by tumor cell clusters. *Science.* 352:167–169. https://doi.org/10.1126/science.aaf6546.
25. Kant Chaudhuri, P., B. Chuan Low, and C. Teck Lim. 2015. Mechanobiology of tumor growth. https://pubs.acs.org/sharingguidelines.
26. Wu, P.-H., D. R.-B. Aroush, …, D. Wirtz. 2018. A comparison of methods to assess cell mechanical properties. *Nat. Methods.* 15:491–498. https://doi.org/10.1038/s41592-018-0015-1.
27. Plodinec, M., M. Loparic, …, C.-A. Schoenenberger. 2012. The nanomechanical signature of breast cancer. *Nat. Nanotechnol.* 7:757–765. https://doi.org/10.1038/nnano.2012.167.
28. Agus, D. B., J. F. Alexander, …, P.-H. Wu. 2013. A physical sciences network characterization of non-tumorigenic and metastatic cells. *Sci. Rep.* 3:1449. https://doi.org/10.1038/srep01449.
29. Marx, V. 2019. Mechanobiology work forcefully for you. *Nat. Methods.* 16:1083–1086. https://doi.org/10.1038/s41592-019-0621-6.
30. Suresh, S. 2007. Biomechanics and biophysics of cancer cells. *Acta Biomater.* 3:413–438. https://doi.org/10.1016/j.actbio.2007.04.002. http://www.sciencedirect.com/science/article/pii/S174270610700061X.
31. Prevedel, R., A. Diz-Muñoz, …, G. Antonacci. 2019. Brillouin microscopy: an emerging tool for mechanobiology. *Nat. Methods.* 16:969–977. https://doi.org/10.1038/s41592-019-0543-3.
32. Nikolić, M., and G. Scarcelli. 2019. Long-term Brillouin imaging of live cells with reduced absorption-mediated damage at 660 nm wavelength. *Biomed. Opt Express.* 10:1567–1580. https://doi.org/10.1364/BOE.10.001567. https://www.osapublishing.org/boe/fulltext.cfm?uri=boe-10-4-1567&id=406961.
33. Staunton, J. R., W. Y. So, …, K. Tanner. 2019. High-frequency microrheology in 3D reveals mismatch between cytoskeletal and extracellular matrix mechanics. *Proc. Natl. Acad. Sci. USA.* 116:14448. https://doi.org/10.1073/pnas.1814271116. http://www.pnas.org/content/116/29/14448.abstract.
34. Staunton, J. R., B. Blehm, …, K. Tanner. 2017. In situ calibration of position detection in an optical trap for active microrheology in viscous materials. *Opt Express.* 25:1746–1761. https://doi.org/10.1364/OE.25.001746. http://www.opticsexpress.org/abstract.cfm?URI=oe-25-3-1746.
35. Santner, S. J., P. J. Dawson, …, F. R. Miller. 2001. Malignant MCF10CA1 cell lines derived from premalignant human breast epithelial MCF10AT cells. *Breast Cancer Res. Treat.* 65:101–110. https://doi.org/10.1023/A:1006461422273.
36. Moshayedi, P., F. Costa Lda, …, K. Franze. 2010. Mechanosensitivity of astrocytes on optimized polyacrylamide gels analyzed by quantitative morphometry. *J. Phys. Condens. Matter.* 22:194114. https://doi.org/10.1088/0953-8984/22/19/194114.
37. Paul, C. D., A. Hruska, …, K. Tanner. 2019. Probing cellular response to topography in three dimensions. *Biomaterials.* 197:101–118. https://doi.org/10.1016/j.biomaterials.2019.01.009. http://www.sciencedirect.com/science/article/pii/S0142961219300158.

38. Kim, J., J. R. Staunton, and K. Tanner. 2016. Independent control of topography for 3D patterning of the ECM microenvironment. *Adv. Mater.* 28:132–137. https://doi.org/10.1002/adma.201503950.

39. Kim, J., and K. Tanner. 2016. Three-dimensional patterning of the ECM microenvironment using magnetic nanoparticle self assembly. *Curr. Protoc. Cell Biol.* 70:25.3.1–25.3.14. https://doi.org/10.1002/0471143030.cb2503s70.

40. Debnath, J., S. K. Muthuswamy, and J. S. Brugge. 2003. Morphogenesis and oncogenesis of MCF-10A mammary epithelial acini grown in three-dimensional basement membrane cultures. *Methods.* 30:256–268. https://doi.org/10.1016/S1046-2023(03)00032-X. http://www.sciencedirect.com/science/article/pii/S104620230300032X.

41. Lee, G. Y., P. A. Kenny, …, M. J. Bissell. 2007. Three-dimensional culture models of normal and malignant breast epithelial cells. *Nat. Methods.* 4:359–365. https://doi.org/10.1038/nmeth1015.

42. Brillouin, L. 1922. Diffusion de la lumière et des rayons X par un corps transparent homogène - influence de l'agitation thermique. *Ann. Phys.* 9:88–122. https://doi.org/10.1051/anphys/192209170088.

43. Nikolić, M., C. Conrad, …, G. Scarcelli. 2018. Noninvasive Imaging: Brillouin Confocal Microscopy. Springer, pp. 351–364.

44. Scarcelli, G., W. J. Polacheck, …, S. H. Yun. 2015. Noncontact three-dimensional mapping of intracellular hydromechanical properties by Brillouin microscopy. *Nat. Methods.* 12:1132. https://doi.org/10.1038/nmeth.3616.

45. Scarcelli, G., R. Pineda, and S. H. Yun. 2012. Brillouin optical microscopy for corneal biomechanics. *Invest. Opthalmol. Vis. Sci.* 53:185. https://doi.org/10.1167/iovs.11-8281. https://iovs.arvojournals.org/data/journals/iovs/932974/z7g00112000185.pdf.

46. Scarcelli, G., P. Kim, and S. H. H. Yun. 2011. In vivo measurement of age-related stiffening in the crystalline lens by Brillouin optical microscopy. *Biophys. J.* 101:1539–1545. https://doi.org/10.1016/j.bpj.2011.08.008. https://www.sciencedirect.com/science/article/pii/S0006349511009507.

47. Pietuch, A., and A. Janshoff. 2013. Mechanics of spreading cells probed by atomic force microscopy. *Open Biology.* 3:130084. https://doi.org/10.1098/rsob.130084.

48. Fischer, M., A. C. Richardson, …, K. Berg-Sørensen. 2010. Active-passive calibration of optical tweezers in viscoelastic media. *Rev. Sci. Instrum.* 81:015103. https://doi.org/10.1063/1.3280222.

49. Fischer, M., and K. Berg-Sørensen. 2007. Calibration of trapping force and response function of optical tweezers in viscoelastic media. *J. Opt. A Pure Appl. Opt.* 112:239–250.

50. Berg-Sørensen, K., and H. Flyvbjerg. 2004. Power spectrum analysis for optical tweezers. *Rev. Sci. Instrum.* 75:594–612. https://doi.org/10.1063/1.1645654.

51. Berg-Sørensen, K., E. J. G. Peterman, …, H. Flyvbjerg. 2006. Power spectrum analysis for optical tweezers. II: laser wavelength dependence of parasitic filtering, and how to achieve high bandwidth. *Rev. Sci. Instrum.* 77:063106. https://doi.org/10.1063/1.2204589.

52. Tolić-Nørrelykke, S. F., E. Schäffer, …, H. Flyvbjerg. 2006. Calibration of optical tweezers with positional detection in the back focal plane. *Rev. Sci. Instrum.* 77:103101. https://doi.org/10.1063/1.2356852.

53. Detect Cell Using Edge Detection and Morphology - MATLAB & Simulink Example. 2020. https://www.mathworks.com/help/images/detecting-a-cell-using-image-segmentation.html.

54. Zhang, J., F. Alisafaei, …, G. Scarcelli. 2020. Nuclear mechanics within intact cells is regulated by cytoskeletal network and internal nanostructures. *Small* 1907688. https://doi.org/10.1002/smll.201907688.

55. Reynolds, N. H., W. Ronan, …, J. P. McGarry. 2014. On the role of the actin cytoskeleton and nucleus in the biomechanical response of spread cells. *Biomaterials.* 35:4015–4025.

56. Kasas, S., X. Wang, …, S. Catsicas. 2005. Superficial and deep changes of cellular mechanical properties following cytoskeleton disassembly. *Cell Motil.* 62:124–132. https://doi.org/10.1002/cm.20086.

57. Golfier, S., P. Rosendahl, …, O. Otto. 2017. High-throughput cell mechanical phenotyping for label-free titration assays of cytoskeletal modifications. *Cytoskeleton.* 74:283–296. https://doi.org/10.1002/cm.21369.

58. Ulrich, T. A., E. M. de Juan Pardo, and S. Kumar. 2009. The mechanical rigidity of the extracellular matrix regulates the structure, motility, and proliferation of glioma cells. *Cancer Res.* 69:4167. https://doi.org/10.1158/0008-5472.CAN-08-4859. http://cancerres.aacrjournals.org/content/69/10/4167.abstract.

59. Pogoda, K., R. Bucki, …, P. A. Janmey. 2017. Soft substrates containing hyaluronan mimic the effects of increased stiffness on morphology, motility, and proliferation of glioma cells. *Biomacromolecules.* 18:3040–3051. https://doi.org/10.1021/acs.biomac.7b00324.

60. Miroshnikova, Y. A., J. K. Mouw, …, V. M. Weaver. 2016. Tissue mechanics promote IDH1-dependent HIF1α–tenascin C feedback to regulate glioblastoma aggression. *Nat. Cell Biol.* 18:1336–1345. https://doi.org/10.1038/ncb3429.

61. Peyton, S. R., and A. J. Putnam. 2005. Extracellular matrix rigidity governs smooth muscle cell motility in a biphasic fashion. *J. Cell. Physiol.* 204:198–209. https://doi.org/10.1002/jcp.20274.

62. Provenzano, P. P., K. W. Eliceiri, …, P. J. Keely. 2006. Collagen reorganization at the tumor-stromal interface facilitates local invasion. *BMC Med.* 4:38. https://doi.org/10.1186/1741-7015-4-38.

63. Wu, P.-H., M. Gilkes Daniele, …, D. Wirtz. 2021. Single-cell morphology encodes metastatic potential. *Sci. Adv.* 6:eaaw6938. https://doi.org/10.1126/sciadv.aaw6938.

64. Solon, J., I. Levental, …, P. A. Janmey. 2007. Fibroblast adaptation and stiffness matching to soft elastic substrates. *Biophys. J.* 93:4453–4461. https://doi.org/10.1529/biophysj.106.101386. https://www.sciencedirect.com/science/article/pii/S000634950771696X.

65. Butcher, D. T., T. Alliston, and V. M. Weaver. 2009. A tense situation: forcing tumour progression. *Nat. Rev. Cancer.* 9:108–122. https://doi.org/10.1038/nrc2544.

66. Yamada, K. M., J. W. Collins, …, S. Wang. 2019. Extracellular matrix dynamics in cell migration, invasion and tissue morphogenesis. *Int. J. Exp. Pathol.* 100:144–152. https://doi.org/10.1111/iep.12329.

67. Paszek, M. J., N. Zahir, …, V. M. Weaver. 2005. Tensional homeostasis and the malignant phenotype. *Cancer Cell.* 8:241–254. https://doi.org/10.1016/j.ccr.2005.08.010.

68. Rigato, A., A. Miyagi, …, F. Rico. 2017. High-frequency microrheology reveals cytoskeleton dynamics in living cells. *Nat. Phys.* 13:771–775. https://doi.org/10.1038/nphys4104.

69. Guck, J., S. Schinkinger, …, C. Bilby. 2005. Optical deformability as an inherent cell marker for testing malignant transformation and metastatic competence. *Biophys. J.* 88:3689–3698. https://doi.org/10.1529/biophysj.104.045476.

70. Hurst, S., B. E. Vos, …, T. Betz. 2021. Intracellular softening and increased viscoelastic fluidity during division. *Nat. Phys.* 17:1270–1276. https://doi.org/10.1038/s41567-021-01368-z.

71. Wirtz, D. 2009. Particle-tracking microrheology of living cells: principles and applications. *Annu. Rev. Biophys.* 38:301–326. https://doi.org/10.1146/annurev.biophys.050708.133724.

72. Urbanska, M., M. Winzi, …, J. Guck. 2017. Single-cell mechanical phenotype is an intrinsic marker of reprogramming and differentiation along the mouse neural lineage. *Development.* 144:4313–4321. https://doi.org/10.1242/dev.155218.

73. Blehm, B. H., A. Devine, …, K. Tanner. 2016. In vivo tissue has non-linear rheological behavior distinct from 3D biomimetic hydrogels, as determined by AMOTIV microscopy. *Biomaterials.* 83:66–78. https://doi.org/10.1016/j.biomaterials.2015.12.019. https://www.sciencedirect.com/science/article/pii/S0142961215010078.

74. Hörner, F., R. Meissner, …, E. Raz. 2017. Holographic optical tweezers-based in vivo manipulations in zebrafish embryos. *J. Biophot.* 10:1492–1501.

75. Hurst, S., B. E. Vos, and T. Betz. 2021. Intracellular softening and fluidification reveals a mechanical switch of cytoskeletal material contributions during division. Preprint at bioRxiv. https://doi.org/10.1101/2021.01.07.425761. http://biorxiv.org/content/early/2021/01/08/2021.01.07.425761.abstract.

76. Schlüßler, R., K. Kim, …, J. Guck. 2022. Correlative all-optical quantification of mass density and mechanics of subcellular compartments with fluorescence specificity. *Elife.* 11:e68490. https://doi.org/10.7554/eLife.68490.

77. Kim, K., and J. Guck. 2020. The relative densities of cytoplasm and nuclear compartments are robust against strong perturbation. *Biophys. J.* 119:1946–1957. https://doi.org/10.1016/j.bpj.2020.08.044.

78. Webb, J. N., J. P. Su, and G. Scarcelli. 2017. Mechanical outcome of accelerated corneal crosslinking evaluated by Brillouin microscopy. *J. Cataract Refract. Surg.* 43:1458–1463. https://doi.org/10.1016/J.JCRS.2017.07.037. https://www.sciencedirect.com/science/article/pii/S0886335017307125.

79. Caponi, S., D. Fioretto, and M. Mattarelli. 2020. On the actual spatial resolution of Brillouin Imaging. *Opt Lett.* 45:1063–1066. https://doi.org/10.1364/OL.385072. http://opg.optica.org/ol/abstract.cfm?URI=ol-45-5-1063.

80. Mattarelli, M., M. Vassalli, and S. Caponi. 2020. Relevant length scales in Brillouin imaging of biomaterials: the interplay between phonons propagation and light focalization. *ACS Photonics.* 7:2319–2328. https://doi.org/10.1021/acsphotonics.0c00801.

81. Kenny, P. A., G. Y. Lee, …, M. J. Bissell. 2007. The morphologies of breast cancer cell lines in three-dimensional assays correlate with their profiles of gene expression. *Mol. Oncol.* 1:84–96. https://doi.org/10.1016/j.molonc.2007.02.004.

82. Haffner, M. C., D. M. Esopi, …, S. Yegnasubramanian. 2017. AIM1 is an actin-binding protein that suppresses cell migration and micrometastatic dissemination. *Nat. Commun.* 8:142. https://doi.org/10.1038/s41467-017-00084-8.

83. Lyons, S. M., E. Alizadeh, …, A. Prasad. 2016. Changes in cell shape are correlated with metastatic potential in murine and human osteosarcomas. *Biol Open.* 5:289–299. https://doi.org/10.1242/bio.013409. https://www.ncbi.nlm.nih.gov/pubmed/26873952.

84. Wu, P. H., J. M. Phillip, …, D. Wirtz. 2015. Evolution of cellular morpho-phenotypes in cancer metastasis. *Sci. Rep.* 5:18437. https://doi.org/10.1038/srep18437. https://www.ncbi.nlm.nih.gov/pubmed/26675084.

85. Wang, P., M. Dreger, …, J. Redondo-Muñoz. 2018. WDR5 modulates cell motility and morphology and controls nuclear changes induced by a 3D environment. *Proc. Natl. Acad. Sci. USA.* 115:8581. https://doi.org/10.1073/pnas.1719405115. http://www.pnas.org/content/115/34/8581.abstract.

86. Wisniewski, E. O., P. Mistriotis, …, K. Konstantopoulos. 2020. Dorsoventral polarity directs cell responses to migration track geometries. *Sci. Adv.* https://doi.org/10.1126/sciadv.aba6505.

87. Zhang, J., X. Nou, …, G. Scarcelli. 2017. Brillouin flow cytometry for label-free mechanical phenotyping of the nucleus. *Lab Chip*. https://doi.org/10.1039/C6LC01443G.

88. Simian, M., and M. J. Bissell. 2016. Organoids: a historical perspective of thinking in three dimensions. *J. Cell Biol.* 216:31–40. https://doi.org/10.1083/jcb.201610056.

89. Kasendra, M., A. Tovaglieri, …, D. E. Ingber. 2018. Development of a primary human Small Intestine-on-a-Chip using biopsy-derived organoids. *Sci. Rep.* 8:2871. https://doi.org/10.1038/s41598-018-21201-7.

90. Huh, D., G. A. Hamilton, and D. E. Ingber. 2011. From 3D cell culture to organs-on-chips. *Trends Cell Biol.* 21:745–754. https://doi.org/10.1016/j.tcb.2011.09.005. https://www.sciencedirect.com/science/article/pii/S0962892411001954.

91. Kim, J., B.-K. Koo, and J. A. Knoblich. 2020. Human organoids: model systems for human biology and medicine. *Nat. Rev. Mol. Cell Biol.* 21:571–584. https://doi.org/10.1038/s41580-020-0259-3.

92. Acerbi, I., L. Cassereau, …, V. M. Weaver. 2015. Human breast cancer invasion and aggression correlates with ECM stiffening and immune cell infiltration. *Integr. Biol.* 7:1120–1134. https://doi.org/10.1039/c5ib00040h.

93. Tanner, K. 2012. Coherent angular motion in the establishment of multicellular architecture of glandular tissues. *Proc. Natl. Acad. Sci. USA.* 109:1973–1978. https://doi.org/10.1073/pnas.1119578109.

94. Bissell, M. J., P. A. Kenny, and D. C. Radisky. 2005. Microenvironmental regulators of tissue structure and function also regulate tumor induction and progression: the role of extracellular matrix and its degrading enzymes. *Cold Spring Harb. Symp. Quant. Biol.* 70:343–356. https://doi.org/10.1101/sqb.2005.70.013.

Biophysical Journal, Volume *121*

Supplemental information

Multimodal microscale mechanical mapping of cancer cells in complex microenvironments

Miloš Nikolić, Giuliano Scarcelli, and Kandice Tanner

Supplementary material

Multimodal microscale mechanical mapping of cancer cells in complex microenvironments

Miloš Nikolić[1,2], Giuliano Scarcelli[2,3], and Kandice Tanner[1, *]

[1]Laboratory of Cell Biology, Center for Cancer Research, National Cancer Institute, National Institutes of Health, USA

[2]Maryland Biophysics Program, IPST, University of Maryland, College Park, MD, USA

[3]Fischell Department of Bioengineering, University of Maryland, College Park, MD, USA

Effect of the nuclear volume fraction on average Brillouin shift of the whole cell

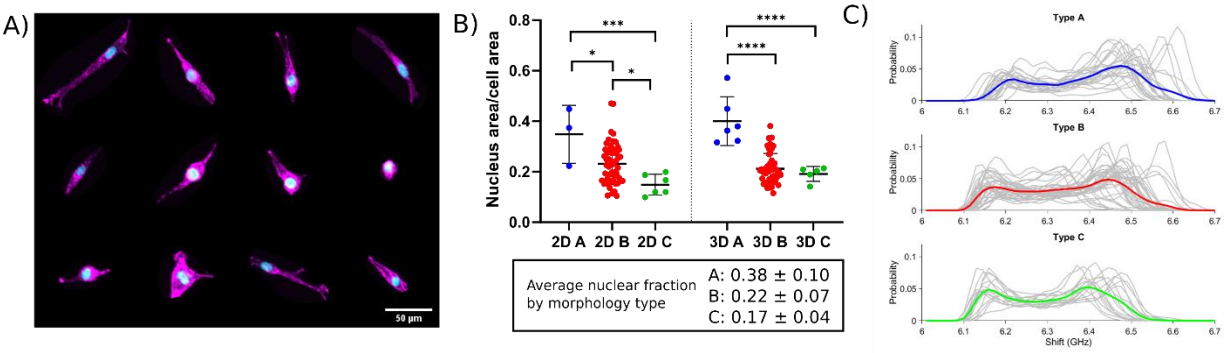

Supplementary Figure 1. Fraction of the nucleus in cell images. (A) Example maximum projection fluorescence images of cells in 2D stained with a nuclear stain (DAPI in cyan) and actin (phalloidin-Atto565 in magenta). The fraction of nucleus is defined as the ratio of the areas of the nucleus and the whole cell which we measured by thresholding the DAPI and phalloidin channels respectively. This analysis was performed in Fiji. (B) Fraction of nucleus in confocal fluorescence images for cells in 2D and 3D conditions. List below is the average nuclear fraction for all cells pooled from both 2D and 3D conditions. (C) Probability distributions of Brillouin shift in all cells from 2D and 3D conditions separated by type. Gray lines indicate individual cells, and colored lines are average distributions.

Supplementary Figure 1 C) shows a heterogeneous mix of individual cells, where the Brillouin shift is distributed with a bimodal distribution per cell. For this dataset, on average the two modes are centered approximately around 6.2 GHz and 6.45 GHz. Previously it has been validated that these two modes correspond to the Brillouin shifts from the cytoplasm and the nucleus respectively (1,2). Assuming that the two modes are Gaussian, the overall mean of the distribution is given by:

$$\mu_{whole\ cell} = f_n\ 6.45\ GHz + (1 - f_n)\ 6.2\ GHz.$$

where f_n is the fraction of voxels inside the nucleus. The difference in the nucleus fraction between type A and type C is about 21% (Supplementary Figure 1 B). Suppose that we measure a theoretical cell with 6.45

GHz shift inside the nucleus and 6.2 GHz inside the cytoplasm, the mean value of the Brillouin shift as a function of f_n is given by:

$$\mu_{whole\ cell} = (0.25\ GHz) f_n\ +\ 6.2\ GHz.$$

In this case the 0.21 change in f_n corresponds to a difference in the mean $\Delta\mu_{whole\ cell} = 52\ MHz$. This is comparable to the measured differences in Brillouin shift across conditions (see Figure 1). It is worth noting that some of the differences in Brillouin shift shown in Figure 3 (e.g. among types within 3D condition) are larger than this value by a factor of 2. This means that not all the differences between different morphology types can be attributed only to the nucleus fraction, although the nucleus plays an important role on the average Brillouin shift of a cell. Therefore, normalizing by multiple relevant parameters is important for understanding the mechanical properties of cells.

Brillouin microscopy at the cell edge

Brillouin microscopy is limited when measuring the cell periphery and very thin protrusions. Voxels at the cell edge that straddle the cell boundary can also contain signal from the surrounding media (3-5). In our data we conservatively exclude those pixels (3.5σ away from the mean of the Brillouin shift of the surrounding medium, and manual corrections when necessary. See methods). Supplementary Figure 2 shows the Brillouin shift of cells as a function of the ratio of pixels at the cell boundary to total number of pixels in the cell. As expected from the morphological analysis which shows that elongated and protrusive cells have lower Brillouin shift (see main text), we find a weak correlation (correlation coefficient -0.31) between the perimeter-area ratio and the Brillouin shift. This is expected because the perimeter-area ratio is related to the traditional morphological parameters: circularity and elongation. The poor value of the coefficient of determination (R^2 = 0.0968) indicates that for any fraction of the boundary pixels in the cell we observe Brillouin shifts with a large variation that cannot be attributed to the amount of boundary pixels in the images.

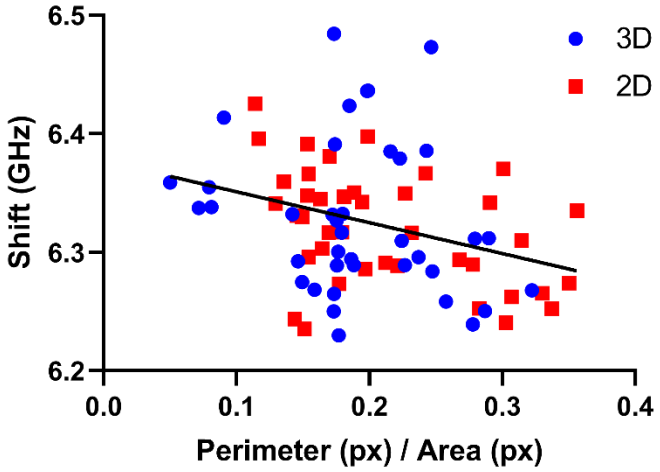

Supplementary Figure 2. Average shift versus the fraction of peripheral pixels in cell image. To confirm that the pixels at the edge of the cell do not affect the overall average shift of the cell, we calculated the fraction of boundary pixels in each Brillouin image. We normalize the number of boundary voxels by the total number of voxels inside the cell used to calculate Brillouin shift (overall cell area in Brillouin map) and plot it against the average Brillouin shift.

Role of cell orientation with respect to the fibrillar topography

Previous work from our lab (6) has shown that cells sense the fibrillar architecture by aligning individual protrusions locally with the fibrillar structure, as well as remodeling the local fibrillar structure. Since cells of type B which have elongated morphology and a preferential axis, also have a higher shift in presence of fibrillar topography (Figure 3. D) we asked if the alignment of the cell axis with the fibrillar architecture correlates with the Brillouin shift of the cell. However, we find no correlation with the Brillouin shift; this could be the result of a poor sensitivity of the measurement due to the high variability of the data especially in thin protrusions or it could suggest that the cells mechanically interact with the fibrillar topography at the level of cell protrusions first, and that the mechanical changes on the level of the whole cell could be downstream effects of that interaction.

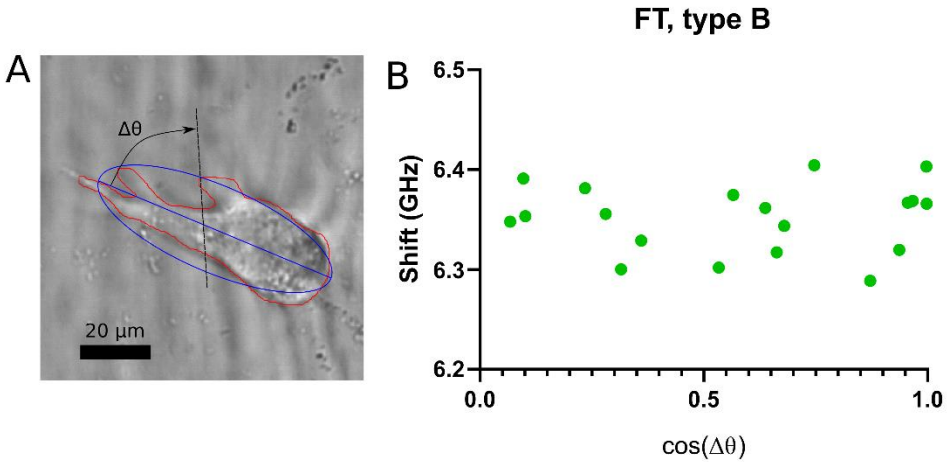

Supplementary Figure 3. Average shift of cell versus alignment with fibrils. (A) Example image of a cell cultured in fibrillar topography. Cell boundary is depicted in red, while the fitted ellipse and the major axis are in blue. The dashed black line is the direction of the local fibrils. Cell alignment is quantified as the cosine of the angle between major axis of the fitted ellipse and the direction of fibrils. (B) Plot of the average Brillouin shift of the cell versus the cell alignment with fibrils. We find no correlation between these two variables (Pearson correlation coefficient = 0.033).

References

1. Zhang, J., F. Alisafaei, M. Nikolić, X. A. Nou, H. Kim, V. B. Shenoy, and G. Scarcelli. 2020. Nuclear Mechanics within Intact Cells Is Regulated by Cytoskeletal Network and Internal Nanostructures. *Small*. n/a(n/a):1907688, doi: 10.1002/smll.201907688, https://doi.org/10.1002/smll.201907688.
2. Zhang, J., X. A. Nou, H. Kim, and G. Scarcelli. 2017. Brillouin flow cytometry for label-free mechanical phenotyping of the nucleus. 17(17), doi: 10.1039/c6lc01443g, http://pubs.rsc.org/en/content/articlepdf/2017/lc/c6lc01443g.
3. Caponi, S., D. Fioretto, and M. Mattarelli. 2020. On the actual spatial resolution of Brillouin Imaging. *Optics Letters*. 45(5):1063-1066, doi: 10.1364/OL.385072, http://opg.optica.org/ol/abstract.cfm?URI=ol-45-5-1063.
4. Caponi, S., D. Fioretto, and M. Mattarelli. 2020. Transition across a sharp interface: Data from Raman and Brillouin imaging spectroscopy. *Data in Brief*. 33:106368, doi: https://doi.org/10.1016/j.dib.2020.106368, https://www.sciencedirect.com/science/article/pii/S2352340920312610.
5. Mattarelli, M., M. Vassalli, and S. Caponi. 2020. Relevant Length Scales in Brillouin Imaging of Biomaterials: The Interplay between Phonons Propagation and Light Focalization. *ACS Photonics*. 7(9):2319-2328, doi: 10.1021/acsphotonics.0c00801, https://doi.org/10.1021/acsphotonics.0c00801.
6. Paul, C. D., A. Hruska, J. R. Staunton, H. A. Burr, K. M. Daly, J. Kim, N. Jiang, and K. Tanner. 2019. Probing cellular response to topography in three dimensions. *Biomaterials*. 197:101-118, doi:

https://doi.org/10.1016/j.biomaterials.2019.01.009,
http://www.sciencedirect.com/science/article/pii/S0142961219300158.